Evolutionary dynamics of phage resistance in bacterial biofilms

Matthew Simmons[1,2†], Matthew C. Bond[2†], Knut Drescher[3,4], Vanni Bucci[1]*, Carey D. Nadell[2]*

[1] Department of Bioengineering, Program in Biotechnology and Biomedical Engineering, University of Massachusetts Dartmouth, N. Dartmouth, MA 02747, USA

[2] Department of Biological Sciences, Dartmouth College, Hanover, NH 03755, USA

[3] Max Planck Institute for Terrestrial Microbiology, D-35043 Marburg, Germany

[4] Department of Physics, Philipps-Universität Marburg, D-35032 Marburg, Germany

† Co-first authors

* Authors for correspondence:

Carey Nadell (carey.d.nadell@dartmouth.edu)
Vanni Bucci (vanni.bucci@umassd.edu)

Abstract

Interactions among bacteria and their viral predators, the bacteriophages, are likely among the most common ecological phenomena on Earth. The constant threat of phage infection to bacterial hosts, and the imperative of achieving infection on the part of phages, drives an evolutionary contest in which phage-resistant bacteria emerge, often followed by phages with new routes of infection. This process has received abundant theoretical and experimental attention for decades and forms an important basis for molecular genetics and theoretical ecology and evolution. However, at present, we know very little about the nature of phage-bacteria interaction – and the evolution of phage resistance – inside the surface-bound communities that microbes usually occupy in natural environments. These communities, termed biofilms, are encased in a matrix of secreted polymers produced by their microbial residents. Biofilms are spatially constrained such that interactions become limited to neighbors or near-neighbors; diffusion of solutes and particulates is reduced; and there is pronounced heterogeneity in nutrient access and therefore physiological state. These factors can dramatically impact the way phage infections proceed even in simple, single-strain biofilms, but we still know little of their effect on phage resistance evolutionary dynamics. Here we explore this problem using a computational simulation framework customized for implementing phage infection inside multi-strain biofilms. Our simulations predict that it is far easier for phage-susceptible and phage-resistant bacteria to coexist inside biofilms relative to planktonic culture, where phages and hosts are well-mixed. We characterize the negative frequency dependent selection that underlies this coexistence, and we then test and confirm this prediction using an experimental model of biofilm growth measured with confocal microscopy at single-cell and single-phage resolution.

Introduction

Because of the sheer number of bacteria and phages in nature, interactions between them are common (1–9). The imperative of evading phages on the part of their hosts, and of accessing hosts on the part of phages, has driven the evolution of sophisticated defensive and offensive strategies by both (10, 11). Phage resistance can evolve very rapidly in well-mixed liquid cultures of bacteria under phage attack (2, 12, 13). This process has been studied for decades, however phage resistance evolution has received little attention in the context of biofilms, in which cells adhere to surfaces and embed themselves in a secreted polymer matrix (14–16). Biofilm growth is thought to be the most common mode of bacterial life, but we are just beginning to understand the mechanistic and ecological details of phage-bacteria interaction within them (9, 17–19).

Microenvironments within biofilms are highly heterogeneous, including steep gradients in nutrient availability, waste product accumulation, oxygenation, and pH, among other factors (20, 21). Furthermore, biofilm structure can impede the movement of solutes and particles that ordinarily would pose grave threats in well-mixed liquid conditions. The extracellular matrix of *Pseudomonas aeruginosa*, for instance, can block the diffusion of antibiotics such as tobramycin (22, 23). Biofilm matrix secreted by *Escherichia coli* and *Pseudomonas aeruginosa* can also alter phage movement (17, 18). The spatial and temporal complexity of biofilm communities make it difficult to anticipate how they will impact phage-bacteria interaction, including the evolution of physiological resistance to phage attack.

Beyond their deep importance to microbial natural history, phages' ability to rapidly destroy susceptible populations makes them attractive as alternative antimicrobials (12, 24, 25). Optimizing phages for this purpose, including an understanding of phage resistance evolution among host bacteria, requires a thorough look at phage-biofilm interactions (26, 27). In particular, biofilm growth may have profound impacts on the relative advantages and disadvantages of phage resistance, which often involves mutations that also carry a growth rate cost, because the spatial structure within biofilms can potentially protect susceptible cells from phage exposure (17, 18, 28). Furthermore, in some conditions, even susceptible bacterial hosts can outrun a phage infection, for example, if host cell grow sufficiently quickly, or if phages are introduced at low multiplicity of infection (28–31). This effect could be significantly altered by the restricted spatial access of phages to their hosts within biofilms.

Here we set out to explore how phage resistance initially evolves in biofilms. To do this we use a combination of spatially explicit simulations and microfluidics-based biofilm experiments with high resolution confocal microscopy. We find that under realistic conditions, biofilm growth promotes the coexistence of phage-susceptible and phage-resistant hosts for much broader parameter space than one would expect in planktonic conditions. Coexistence is supported by a spatially-driven mechanism of negative frequency dependent selection, which we investigate in detail. This result is robustly supported by high-throughput simulations and experiments interrogating phage-bacteria interactions within live biofilms.

Results

In biofilm environments, the population dynamics of bacteria and their lytic phages are driven by many processes, including bacterial growth, cell-cell shoving, solute advection/diffusion, phage-host attachment probabilities, phage lag time and burst size, and phage advection/diffusion, among others (9, 28). To study phage resistance evolutionary dynamics, we expanded a simulation framework previously developed by ours groups that captures the biological and solute/particle transport processes inherent to biofilm communities (28). The framework is customized to implement tens to hundreds of thousands of discrete bacteria and phages in explicit space, and to simulate genetically susceptible and resistant bacterial sub-populations (see Materials and Methods). Briefly, cells are inoculated onto a solid surface at the bottom of a 2-D space with lateral periodic boundary conditions. Growth-limiting nutrients diffuse from a bulk liquid layer towards the biofilm front, where they can be depleted due to consumption by cells (Figure 1A). The biofilm surface erodes in a height-dependent manner, reflecting the increase in shear rate with distance from the surface (32). After a pre-set interval of biofilm growth, phages are introduced

to the system in a pulse distributed along the biofilm's upper surface (varying the timing of phage pulses had no qualitative impact on the results, see Materials and Methods). Phages can associate with cells in the biofilm and initiate infections, or be released into the surrounding liquid, where they diffuse for a full simulation iteration cycle prior to being swept out of the system by advection. Phage movement rules are described in detail in Materials and Methods.

To begin, we constrained our simulations using experimentally measured parameters for bacterial growth, phage replication, and nutrient diffusion (See Table S1), using measurements for *E. coli* and its lytic phage T7 (the

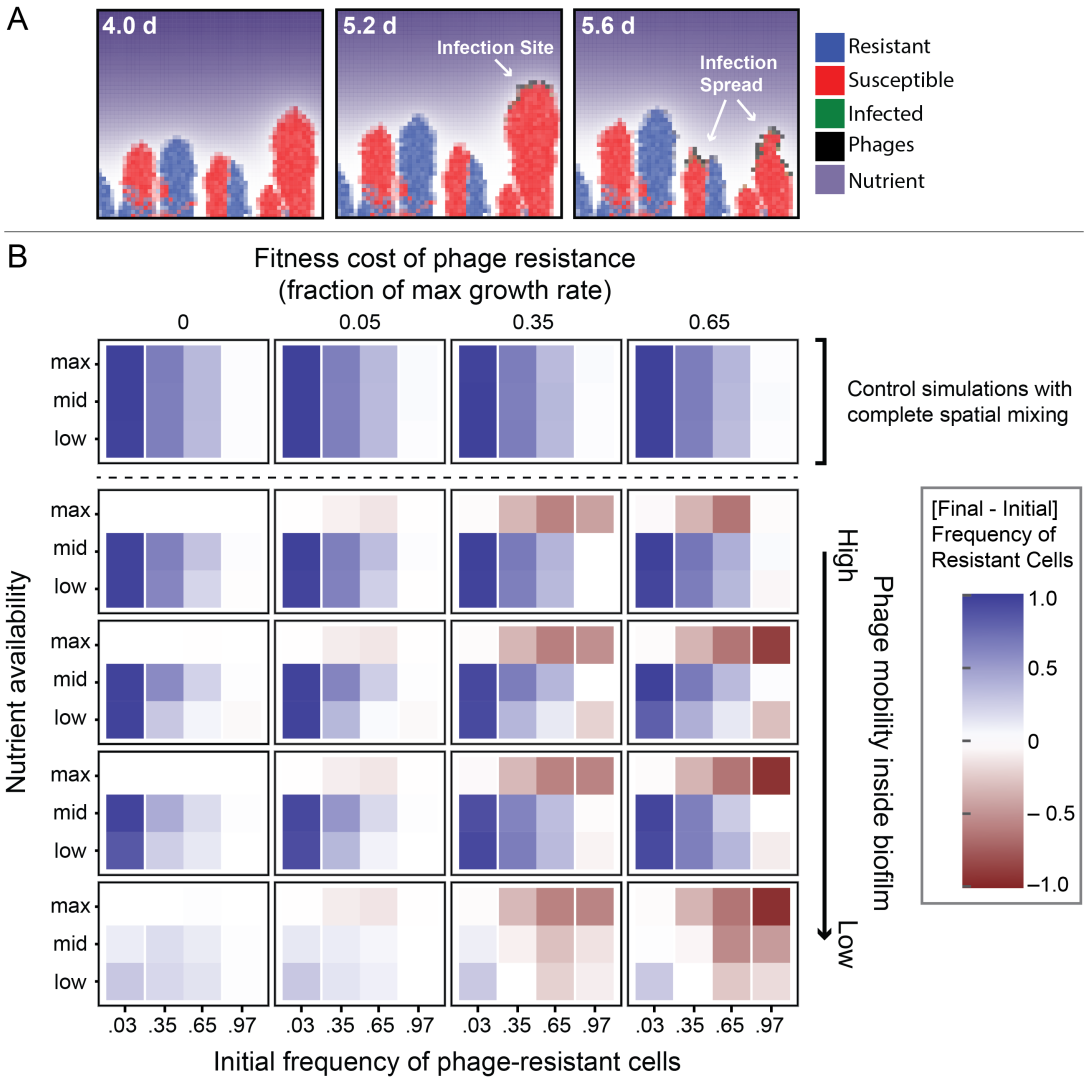

Figure 1. A) An illustration of the basic growth, nutrient diffusion, and phage infection processes inherent to the biofilm simulation framework. B) The influence of phage resistance cost, nutrient availability, initial population composition, and phage mobility on the evolutionary dynamics of phage-resistance. Simulation parameters were constrained using measured values for *E. coli* and phage T7. Within each bold-outlined box, each square denotes the mean difference in final minus initial frequency of phage-resistant cells at simulation end points. Note that the initial frequency sets how far the resistant strain's frequency can shift in either direction and thus the range of potential intensity values for each square. Each row indicates the shape of selection for phage resistance, with all-blue (dark blue on left and light blue on right) indicating positive selection and all-red (light red on left and dark red on right) indicating negative selection. When a row has blue squares on the left and red square on the right, each strain can invade when initially rare, which is the defining signature of long-term coexistence.

same species used in our experiments, see below). We explored the impact of factors that are likely to vary in natural environments where phage-biofilm interactions occur. The first is nutrient availability, which controls overall biofilm expansion rate and influences inter-strain spatial structure and biofilm surface shape (33, 34). We also varied the fitness cost of phage resistance, and the ability of the biofilm population to limit phage diffusion. Lastly, for any given combination of these parameters we also varied the initial population ratio of susceptible to resistant host bacteria. By varying initial fractions in this way, we could test for the invasibility of rare mutants and assess the stability properties of emergent population steady states. For example, if resistant cells always increase (or decrease) in frequency regardless of their initial fraction, we can infer that they are being positively (or negatively) selected. On the other hand, if they increase when initially rare but decrease when initially common, then we can infer that resistant and susceptible cells will tend toward coexistence (35). For comparison, we also include simulations with no spatial structure, where all cells and phages are allowed to interact randomly. The results of this system exploration are shown in Figure 1B (Figure S1 illustrates the corresponding variance in simulation outcomes), and we discuss the major outcomes in turn below.

Phage resistance is strongly favored in well-mixed conditions

Our spatially homogenous control simulations, which were also parameterized according to measured growth features of *E. coli* and phage T7, showed that phage-resistant host cells have a strong fitness advantage over phage-susceptible hosts under phage exposure, always increasing to fixation in the population (Figure S2). This outcome was independent of the nutrient supply or the initial frequency of phage-resistant cells in the population, implying that for our realistic parameterization there is no predicted coexistence of phage-resistant and -susceptible cells in well-mixed conditions (4, 36, 37).

Phage resistance is disfavored when biofilms can outgrow phage epidemics

When nutrient supply is saturating (denoted by "max" in Figure 1), such that biofilms expand faster than phage infections can penetrate by killing susceptible cells, then phage predation does not impose a substantial influence on population composition (SI Video 1). Instead, under high nutrient influx conditions, biofilms out-grow phage epidemics in a manner related to that observed by Eriksen et al. (29). In these conditions bacteria experience a simple growth race in which replication rate is the most important fitness currency. As can be seen in the top row

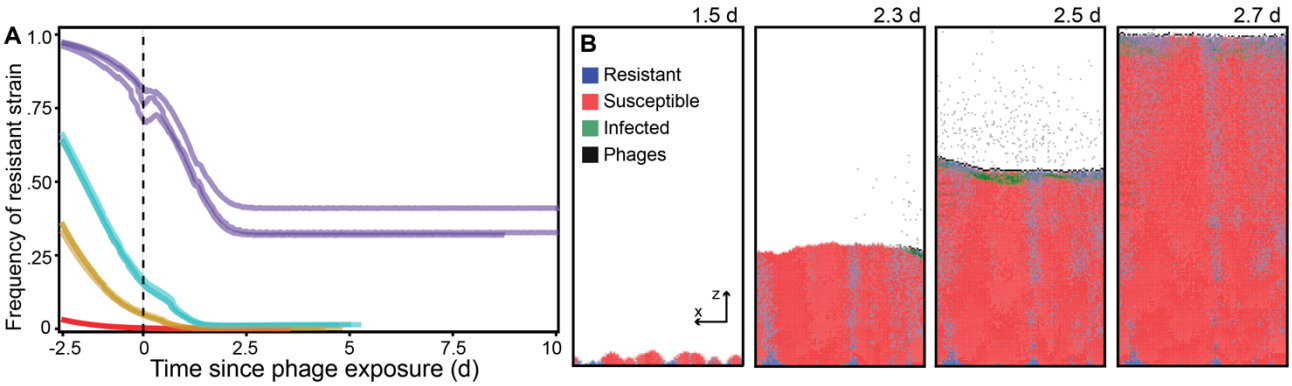

Figure 2. Population dynamics of phage-resistant and susceptible bacteria within biofilms saturated with nutrients (noted as "max" in Figure 1) such that all cells are growing at or near maximal rates at all times. (A) The frequency of resistant cells is shown from different starting conditions; varying trace colors correspond to the initial frequency of resistant cells (red: 0.05; orange: 0.35; teal: 0.65; purple: 0.95) and are meant to assist in visualization. Some runs were halted before the 10 d mark because of limitations on shared computational clusters, but these had all reached steady state. For the runs shown here, the fitness cost of phage resistance is 0.35, and phage mobility through the biofilm is moderate. (B) An example of the biofilm simulation space during phage infection in biofilms with saturating nutrient conditions. Here biofilms grow with smooth, rapidly-advancing fronts that out-strip phage propagation. In this example, the fitness cost of phage resistance is 0.35, phage mobility is moderate, and the initial frequency of resistant bacteria is 0.65.

of each block within our parameter sweep (Figure 1), we observe neutral competition between phage-susceptible and -resistant cells when the cost of resistance is zero (SI Video 1), and as the cost of resistance increases, the resistant strain suffers a lower and lower growth rate such that they are selected against (Figure 2, SI Video 2).

With decreasing phage diffusion and moderate or low nutrient supply, phage-resistant and phage-susceptible cells coexist

When nutrient supply is not saturating (denoted as "mid" and "low" nutrient availability in Figure 1), biofilm growth and overall morphology change considerably. The biofilm surface structure tends to be rough with different cell lineages segregated in space, a result of strong restriction of cellular growth to only an outer active cell layer. This limited active layer growth occurs due to depletion of nutrients before they can reach the full biofilm depth (34, 38–40). This feature of nutrient-limited biofilms generates rough surface structure by amplifying initially small irregularities in surface height and causes strain segregation due to strong bottlenecks in population composition along the advancing front (38, 41–43). In these conditions, phage infection can out-strip biofilm expansion. Inspection of the rows within each block of Figure 1 indicates that for most of "mid" and "low" nutrient parameter space, resistant cells and susceptible cells can both increase in frequency when initially rare. In other words, phage-susceptible and phage-resistant bacteria undergo negative frequency-dependent selection whenever 1) phages are not able to diffuse freely, and 2) the biofilm as a whole is not growing so quickly as to out-run the spread of phage-mediated killing of susceptible cells. These population dynamics imply that the long-term outcome of competition between resistant and susceptible cells is coexistence (35, 44–46). We next explored the origin of this negative frequency-dependence: in the face of lytic phage attack and limited phage movement in biofilms, why do phage-resistant cells fare well when rare, but fare poorly when common?

Clearance effect – We found that when phage-resistant cells are rare within the population that nucleates a biofilm, there are likely to be only sparse clusters of them due to simple constrains on cell movement. As a result, when phages enter the system, they have unfettered access to susceptible hosts that occupy the majority of space, and the propagating infection eliminates most or the all of the susceptible population. After this clearance, the few remaining phage-resistant cells have an abundance of open space into which they can grow to re-seed the entire biofilm population, approaching fixation in the process (Figure 3A,B, SI Video 3).

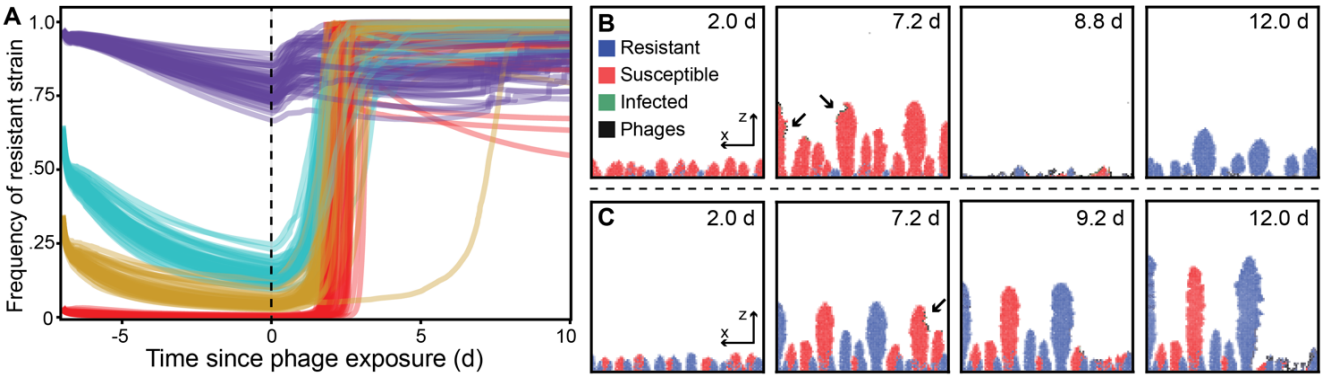

Figure 3. Population dynamics of phage-resistant and susceptible bacteria within biofilms with low nutrient availability (denoted by "low" in Figure 1). (A) The frequency of resistant cells is shown from different starting conditions; varying trace colors correspond to the initial frequency of resistant cells (red: 0.05; orange: 0.35; teal: 0.65; purple: 0.95) and are meant to assist in visualization. For the runs shown here, the fitness cost of phage resistance is 0.35, and phage mobility through the biofilm is low. (B,C) Under limiting nutrient conditions, biofilms grow with rough fronts and spatially segregated cell lineages. When resistant cells are initially a minority (B), susceptible cells are highly exposed to phages and largely killed off, allowing resistant cells to re-seed the population. When resistant cells are initially more common (C), and phages cannot diffuse freely through the biofilm, susceptible cells are spatially protected from phage exposure. In (B) and (C), arrows indicate initiation points of phage infections.

Phage blocking – When phage-resistant cells initiate biofilms in the majority, on the other hand, phage-susceptible cells tend to grow in clusters enveloped within multiple layers of phage-resistant cells, or in strain-segregated towers adjacent to towers of resistant cells. If phages are able to diffuse freely through biofilm biomass, then this spatial arrangement offers no protection to susceptible cells, but once phage diffusion is even moderately impeded by the presence of biofilm, then susceptible cells gain protection from phage exposure. This occurs because phages are sequestered to a degree within clusters of resistant cells, and because phages in released into the liquid phase are blocked from long-range movement to towers of susceptible cells by towers of resistant cells standing in the way. The lower the frequency of susceptible cells in the initial inoculum, the stronger the effect of these spatial protection mechanisms. In this scenario, if there is no cost to resistance, then susceptible and resistant cells compete neutrally. However, if there is a fitness cost to resistance, then susceptible cells have an intrinsic growth rate advantage, and they increase in frequency if they are initially rare (Figure 3A,C, SI Video 4).

Experimental model of phage resistance evolutionary dynamics

Our simulation results lay out a spectrum of potential population dynamics between biofilm co-dwelling cells that are resistant or susceptible to lytic phage attack. In particular, we predict a strong trend toward coexistence of phage-susceptible and phage-resistant cells in nutrient supply conditions that best reflect empirical conditions (low to moderate nutrient supply). Here we set out to test this prediction using an experimental model of biofilm growth and lytic phage infection tracking. Biofilms of *E. coli* were cultivated in microfluidic devices, including co-cultures of wild type AR3110 (WT), and an isogenic strain harboring a clean deletion of *trxA* (see Materials and Methods). The Δ*trxA* null mutant lacks thioredoxin A, which is an essential DNA processivity factor for the lytic phage T7. The Δ*trxA* mutant therefore does not allow for phage amplification, while WT is susceptible (47). To monitor the infection state of cells, we use a previously engineered strain of phage T7 containing *sfGFP* inserted to its genome under strong constitutive expression (18).

The *E. coli* experimental biofilms were cultivated in microfluidic devices composed of a chamber molded into PDMS, which was then bonded to a glass coverslip for imaging on an inverted microscope. In different runs of the experiment, mimicking our simulation approach, we inoculated the glass bottom of flow devices with varying ratios of phage-susceptible and -resistant bacterial cells; allowed biofilms to grow undisturbed for 48 hours; and then subjected them to a pulse of high-density phage suspensions (Figure S3; Materials and Methods). Biofilm populations were then imaged by confocal microscopy at regular intervals until the relative abundances of WT

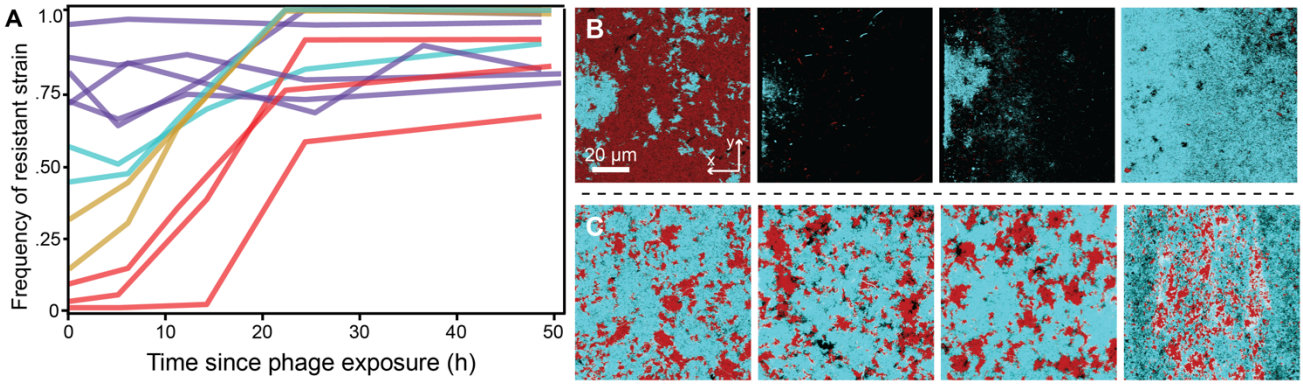

Figure 4. Experimental test of model predictions. Biofilms containing mixtures of phage T7-susceptible AR3110 *E. coli* and a phage T7-resistant null mutant carrying a deletion of *trxA* were grown for 24 hours before administering a pulse of phages to the two-strain biofilm population. (A) Population dynamics traces showing the frequency of phage-resistant *E. coli* as a function of its initial population frequency. Varying trace colors are shown to assist in visualization. (B, C) Time series of phage-resistant (blue) and phage-susceptible cells (red) following a pulse of phages into the chambers. Panels from left to right show biofilms at ~ 0, 12, 24, and 48 hours post phage exposure. Each image is an x-y optical section from a stack of images covering the whole biofilm volume, taken by confocal microscopy.

(susceptible) and Δ*trxA* (resistant) host cells stabilized, indicating that the population had settled into a steady state. For each imaging session, the entire biofilm volume was captured in successive optical sections.

We found that when phage-resistant cells were initially uncommon, susceptible cells were killed off by phage exposure and mostly cleared out of the chambers, opening new space into which resistant cells could grow for the remainder of the experiment (Figure 4A,B). This effect was strongest when resistant cells initiated at a frequency of 0.25 or less, but was still observable for intermediate (0.5/0.5 resistant/susceptible) initial conditions. On the other hand, when phage-resistant cells were initially common (75% of the population, or more), the relative fraction of resistant and susceptible host bacteria did not substantially change following phage treatment (Figure 4A,C).

Our experimental results thus gave a strong match to the simulation predictions for moderate phage mobility, and moderate or low nutrient supply (Figure 1). Furthermore, the mechanistic basis of these outcomes was the same as those observed in our simulations, including a clearance effect when resistant cells are initially rare. In this condition, susceptible cells are fully exposed to phages and die out; the remaining resistant cells then re-seed the population (Figure 4B). Our experiments also confirmed the phage blocking effect: when resistant cells are initially common, they often sequester phages away from susceptible cells, which are then protected from phage exposure and manage to remain near their initial frequency in the population (Figure 4C). To further test this inference, we introduced fluorescently-labelled T7 phages to biofilms initiated with a majority of resistant bacteria, and directly observed that these phages often could not reach isolated pockets of susceptible cells (Figure 5, additional replicas in Figure S4). Because resistant and susceptible cells both increase in frequency when they are initially rare, the expected long-term outcome is coexistence of the two types of bacteria, even when there is little or no fitness cost for phage resistance.

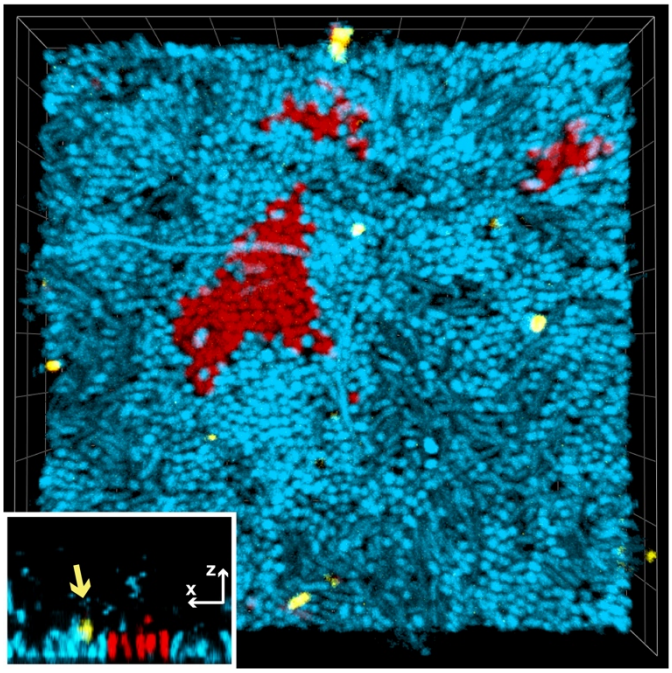

Figure 5. Demonstration of phage blocking in an experimental biofilm of phage-resistant (blue) and phage-susceptible (red) *E. coli*. Purified phages stained with Alexafluor (yellow) were added to 48 h biofilms in which resistant cells were inoculated as 95% of the founding population. The central image is a top-down view of a 3-D rendering measuring 50μm x 50μm x 15 μm [L x W x D]. The inset image is a projection of a vertical slice through a 3-D volume. The yellow arrow points to an immobilized phage on a cluster of resistant cells.

Discussion

Our work here provides a foundation for understanding how phage infection and diffusion within biofilms determine the evolutionary dynamics of phage resistance. Using simulations with extensive parameter sweeps, we found that in the limit of saturating nutrient supply, when biofilm growth is exceedingly fast relative to phage infection, biofilms can "shed" a phage epidemic from their rapidly advancing front. In these conditions, which are likely met under limited circumstances of very rich nutrient availability, phage resistance provides little or no advantage. On the other hand, when nutrient supply conditions are more realistic, such that biofilm-dwelling cells cannot simply out-grow the spread of phages, there is a strong trend toward negative frequency-dependent selection for phage resistance/susceptibility that is highly robust to parameter changes.

The origins of frequency-dependent selection are tied to the cell movement constraints and competition for space in biofilms. When phage-resistant bacteria are initially rare, introduced phages have open access to susceptible hosts, which are mostly or entirely killed, leaving empty space for the residual resistant cells to re-inoculate the population (clearance effect). On the other hand, when phage-resistant bacteria are initially common, they create barriers between phages and clusters of susceptible cells, in addition to sequestering phages from the liquid phase. So long as there is limited diffusion of phages through biofilm biomass, this spatial arrangement provides protection to susceptible cells (phage blocking), whose population frequency can then drift or increase significantly depending on the fitness costs of phage resistance. The experimental results were an excellent match to these predictions, as we could observe both the clearance and phage blocking effects, depending, as anticipated, on the initial fraction of resistant and susceptible bacterial cells. Because both resistant and susceptible cells are particularly successful when initially rare – as would be the case when one is a mutant singleton or small cell cluster – the prediction is for long-term coexistence of the two strains.

Our results provide a first glimpse into the evolutionary dynamics of phage resistance in biofilms with microscopically resolved insight into the underlying cell-cell and cell-phage interactions. These observations in turn have several general implications. We anticipate that the arms race of phage attack and host defense can have a very different landscape in biofilms as opposed to planktonic populations (2, 5, 7, 19, 48). A rich history of research has shown that phages can rapidly eliminate susceptible host cell populations in mixed liquid culture, leading to strong selection for phage resistance (2–4, 37). In biofilms, by contrast, our results predict widespread and easily-maintained polymorphism in phage resistance ability. This kind of standing variation can arise due to minority advantage (i.e., kill-the-winner) mechanisms (49–52), in which phages or other parasites are selected to target the most abundant constituent strains of a population; notably, the mechanism we describe here is distinct but complementary: susceptible cells in the minority are unlikely to be exposed to phages in the first place, as they are usually shielded by resistant cells blocking phage diffusion. The arms race between phages and host bacteria, therefore, is likely to take different evolutionary trajectories that move at slower speeds that those typically observed in liquid culture.

On the basis of simulations and experiments we can also make predictions about the spatial architectures of phage-host interaction that are particular to biofilm environments. Prior work from our groups and others have shown that phages can be immobilized within the biofilm matrix, where they are blocked from gaining access to otherwise susceptible cells (17, 18). Our observations here indicate that whenever phage movement is limited within biofilms, it is likely that the extracellular matrix (which is modeled implicitly here as the factor controlling phage diffusion) contains phages which are blocked from host access but not necessarily inert; they remain a threat to susceptible cells after the dispersion of biofilms due to mechanical disturbance or induced by bacteria themselves after depleting local nutrient supplies (53, 54). The implications of this prediction are a subject for future work.

Our results also bear on the efficacy of phage therapies, for which one of the most promising potential benefits is selective elimination of target pathogens from a community of otherwise commensal or beneficial microbes (12, 25, 51, 55, 56). This is a particularly compelling advantage relative to broad-spectrum antibiotics that can kill off not just the target pathogen but also many other members of a patent's microbiota, sometimes with severe side effects. Our work suggests that while it might be possible to completely eliminate target bacteria with lytic phages from a mixed population, the success of this approach might depend heavily on the community composition and spatial structure. Phage-susceptible cells, when a minority of the population, are much harder to target and can coexist with resistant cells due to the protective effects of phage diffusion blocking in mixed biofilms. It should be noted, however, that our work here only examines two strains of the same species, and whether these conclusions apply to multi-species consortia (57), whose biofilm architectures can differ substantially, is an important topic for further work.

The models developed here do not address the possibility of refuges created by quiescent bacteria in the basal layers of biofilms where nutrients have been depleted (48). This did not appear to be an important feature of

our experimental biofilms, which agreed well with simulation predictions. However, quiescent cells could potentially be significant in other conditions, especially for cell groups that accumulate thicker mats with large, nutrient-starved populations in their interior. We also do not implement ongoing mutations in the different bacterial and phage strains residing in biofilms, using instead strains that are fixed in either the phage-susceptible or -resistant state to examine short term population dynamics. This approach allows us to infer longer-term evolutionary dynamics, but does not address the possibility of bacteria harboring different degrees of phage resistance bearing different fitness costs, or different mechanisms of phage resistance that could interact in unanticipated ways (such as abortive infections (10), or CRISPR adaptive immunity (58)). Lastly, and importantly, we omitted from our simulations and experiments the possibility of lysogenic infections, in which the phage genome is inserted to the chromosome of the host organism, emerging to replicate and produce new phages when the host is under duress. Lysogenic phages present a wide diversity of potential outcomes, especially considering that they can impart new phenotypes to their bacterial hosts. Tackling the challenge, both theoretically and experimentally, of how lysogenic phages enter, alter, and evolve within multispecies microbial communities is an important area for future work.

Author Contributions

CDN conceived the project; CDN and VB designed simulations and experiments. MKS wrote the simulation framework and performed simulation data collection. MCB performed experiments and image processing of microscopy data. MKS, MCB, KD, VB, and CDN analyzed data. CDN and VB wrote the paper with input from all authors.

Acknowledgements

We are grateful to Will Harcombe, Wolfram Möbius, Kai Orton, and Sara Mitri for helpful comments on earlier versions of the manuscript. MCB is supported by a GANN Fellowship from Dartmouth College. KD receives grant support from the European Research Council (StG-716734), the Deutsche Forschungsgemeinschaft (SFB 987), and the Behrens-Weise-Foundation. VB is supported by NSF ABI 1458347), and a UMass President Science and Technology award. CDN and VB are supported by NSF MCB 1817342). CN is also supported by a Burke Award from Dartmouth College, a pilot award from the Cystic Fibrosis Foundation (STANTO15RO), and NIH grant P20-GM113132 to the Dartmouth BioMT COBRE.

Materials and Methods

Phage-biofilm modeling simulation framework:

The simulation framework used for this study is an updated and expanded version of a modeling approach developed in Simmons et al. (28). The major changes include a new implementation of bacteria as individual particles rather than a homogeneous biomass, and a new implementation of phage diffusion, detailed below. The simulations are built on a grid-based approach for tracking bacteria, phages, and solute concentrations; spatial structure in the system is thus resolved at the level of grid nodes (which are 3μm x 3μm for the simulations described in this paper). Within a grid node, bacteria and phages are tracked individually but assumed to interact randomly. The same grid system is used to calculate nutrient diffusion from a bulk layer above the biofilm toward the cell group surface, where it is consumed by bacteria (33, 40, 59).

As a result of nutrient consumption on the biofilm's advancing front (Figure 6), nutrient gradients are created with high nutrient availability in the outer cell layers and lower nutrient availability with increasing depth into the biofilm interior (particularly for the "low" and "mid" conditions in Figure 1 of the main text). Cells near the liquid interface grow maximally, while cells deeper in the biofilm interior grow relatively slowly. Fluid flow is modeled implicitly; following prior literature, we allow the biofilm to erode along its outer front at a rate proportional to the square of the distance from the basal substratum (described in detail in Simmons et al. (28)). Further, any phages that depart from the biofilm into the surrounding liquid are advected out of the simulation space within one iteration cycle, which is approximately 7-8 minutes in simulation time (see below).

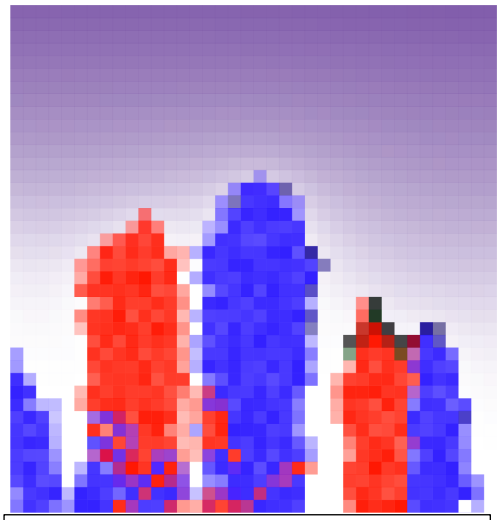

Figure 6. A close view of the grid compartment structure of our simulation framework, illustrating distributions of phage resistant (blue) and susceptible cells (red). Phages (black) can infect and kill susceptible cells; they can be sequestered by resistant cell biomass, but cannot kill them. Gradients of nutrient availability (purple) form due to depletion along the advancing front of the biofilm. Each grid box is 3μm x 3μm.

The simulation framework was written in an object-oriented style. A simulation object is defined *via* the space of the system, number and properties of implemented grid node containers, biological behaviors of bacteria and phages, one-time events (e.g. phage pulse), and simulation exit conditions. Briefly, the space of the system specifies physical information such as physical size and length scale of the grid node array in which cells, phages, and solutes are implemented. The containers hold the information about each modeled individual present in the system. Behaviors describe a container's interactions with anything else including other containers, space, or time. Events are one-time-use behaviors including the inoculation of the system with bacteria or pulses of phages into the simulation space.

Simulations were initiated by first defining the types of container contents, including both bacterial strains/species of interest (phage-susceptible and phage-resistant), phage-infected bacteria, phages, and the growth substrate as a solute. This process includes specifying values for basic biological and physical parameters in the system (e.g. bacterial growth rate, phage infection rate per host-virus contact, phage lag time, phage burst size, nutrient diffusivity, and others; the full list of parameter values and their measurement origins is provided in Table S1). After containers are established in each simulation instance, the simulation proceeds through inoculation of the two bacterial species on the substratum. Phages were not introduced at the outset of simulations but rather at a set time after bacteria were permitted to grow, as described in the main text. Simulations proceed along the following cycle of steps:

1. diffusion of the nutrient substrate,
2. biomass growth and division,
3. erosion of biomass,
4. phage movement,
5. detachment of biomass,
6. phage infection,
7. lysis of infected bacteria,
8. biofilm relaxation ('shoving'),
9. detachment of bacteriophage.

The order of simulation steps described has no impact on outcomes, with one exception: phage movement cannot be executed between biomass detachment and phage detachment, as this would lead to the phage inappropriately freely moving after a significant biomass detachment event.

Phage mobility implementation: All processes describing phage-bacteria dynamics are equivalent to those presented in Simmons et al. (28) with one exception pertaining to the methods of computing phage entry and exit from the biofilm bacterial volume. This new approach is described in detail below.

Previously, we analytically solved the diffusion equation to approximate the phage density as a function of location in the biofilm. Here, in order to accommodate for possible biological heterogeneity in bacteriophage dynamics (60, 61), we introduced an algorithm for calculating phage movement by modeling each phage's individual Brownian motion as a random walk. To account for the effect of the biofilm matrix on phage movement, we introduced a new model parameter (the interaction rate, *I*) controlling the diffusivity of phages through areas of simulation space occupied by bacterial biomass (28).

The improved implementation of phage mobility operates as follows. For each phage: 1) We first calculate the number of potential steps that could be taken in the next time interval as: $n = D_p\ dt\ /\ (2\ dl^2)$, where dl is the grid length scale, D_p is the diffusivity of the phage, and dt is the integration time step. 2) Next we calculate the probability of interaction with the bacterial biomass at each current location as $p = 1 - exp(dt\ \Sigma\ I)$, where I is the interaction rate parameter. If a random number drawn from a uniform distribution (0,1) is smaller than p, then the phage has interacted with biofilm biomass in the current location, and hence has stopped moving. If the phage has not interacted, a direction is randomly chosen and the phage moves to that location on the grid. As the interaction rate, I, increases, the ability of the phage to diffuse through biomass decreases (e.g., p tends to 1), which is a per-individual-phage representation of the phage impedance parameter previously described by Simmons et al. (28). Once the phage stops moving, we evaluate the remaining time as $dt * s/n$, where s is the number of steps taken, from 0 to n, and use it in the infection step.

As noted above, phage mobility outside of a biofilm is modeled by implicitly implementing advection in the vicinity of the biofilm front. Any phages released from the biofilm front can diffuse through the surrounding liquid volume in the interim of the same iteration cycle, which is ~7-8 minutes in simulation time. For a phage diffusivity of 3.82 x 10^{-7} cm^2/s (see Table S1), this persistence time allowed phages in the liquid outside the biofilm to diffuse ~100 μm before being advected out of the system.

Details on simulation initial conditions and execution of parameter sweeps: Where possible, biological and physical parameters of the simulation system were constrained according to experimentally measured values for *E. coli* and phage T7, which were the focal species of our experiments as well (see Table S1). Following our previous biofilm dynamics simulation work (28, 34, 62), each simulation starts with an initial ratio of phage-susceptible and -resistant strains on the solid substratum, and these two strains compete for access to space and growth-limiting nutrients that diffuse from a bulk layer above the biofilm. After t = 7 d (low nutrient supply) or t = 2 d (mid/high nutrient supply) of biofilm growth, a pulse of bacteriophages was added to the top layer of the growing biofilm, simulating the arrival of phage bursts that were released somewhere upstream in the larger flow system. Repeating our simulation parameter sweeps with earlier (Figure S5) or later (Figure S6) phage inoculation had no effect on the qualitative outcomes. Two phage inoculation methods were tested. The first was a "spray" of phages in the area just above the biofilm outer surface: empty grid points 10 μm above biomass along the outer biofilm exterior were populated with three viruses. The second approach to phage inoculation was a 100-virion pulse at a single position 10 μm above the highest point in the biofilm. Data reported in Figure 1 correspond to simulations obtained using the first method, but we confirmed that the core results do not qualitatively vary when the method of inoculating phages at a single point in space is used (Figure S7).

Simulations were run until one of two different exit conditions was reached: either bacterial species going to fixation, or the simulation ran to a pre-specified end point (time of infection + 10 days). Simulations were run for three different nutrient supplies (see Figure 1) corresponding to three distinct biofilm morphologies ("max"

nutrient supply leading to biofilms with smooth fronts and relatively mixed cell lineages, and "mid" and "low" nutrient supply, which led to rough surface fronts and stronger cell lineage spatial separation) (38, 42). To vary nutrient supply, the bulk substrate, diffusivity, and boundary layer height were modified. Simulations were run also for four distinct fitness cost levels of phage resistance, and for five different values of the interaction rate parameter, which effectively varied phage mobility through biofilms from freely-moving to severely-impeded immediately upon biofilm contact (see main text). For each combination of parameters, except for those in the "max" nutrient supply condition, we ran 50 simulations with different random seeds. The max nutrient supply conditions have 3 simulation runs each, as they have a much higher computational demand. These simulations were also generally cut off early on the compute cluster, due to the time they would take to execute and the observation that they had reached a steady state with respect to phage infection and population composition (see Figure 2 and SI Videos 1 and 2). For the well-mixed control simulations whose results are shown at the top of Figure 1, we disabled all spatially dependent behaviors: substrate diffusion, biomass erosion, biofilm detachment, biofilm relaxation, phage detachment. For each well mixed parameter combination, we ran 6 simulations.

Experimental Materials and Methods:

Bacterial Strains. Both strains used in this study are *E. coli* AR3110 derivatives, created using the lambda red method for chromosomal modification (63). The Δ*trxA* deletion strain was created by amplifying the locus encoding chloramphenicol acetyltransferase (*cat*) flanked by FRT recombinase sites target sites, using primers with 20bp sequences immediately upstream and downstream of the native *trxA* locus. The FRT recombinase encoded on pCP20 was used to remove the *cat* resistance marker after PCR and sequencing confirmed proper deletion of *trxA*. The wild type *E. coli* AR3110 was engineered to constitutively express the fluorescent protein mKate2, and the *trxA* null mutant was engineered to constitutively produce the fluorescent protein mKO-κ. These fluorescent protein expression constructs were integrated in single copy to the *attB* locus on the chromosome, and they allowed us to visualize the two strains and distinguish them in biofilm co-culture by confocal microscopy.

Biofilm growth in microfluidic channels. Microfluidic devices were constructed by bonding poly-dimethylsiloxane (PDMS) castings to size #1.5 36mm x 60mm cover glass (ThermoFisher, Waltham MA) (64, 65). Bacterial strains were grown in 5mL lysogeny broth overnight at 37°C with shaking at 250 r.p.m. Cells were pelleted and washed twice with 0.9% NaCl before normalizing to $OD_{600} = 0.2$. Strains were combined in varying ratios (see main text) and inoculated into channels of the microfluidic devices. Bacteria were allowed to colonize for 1 hour at room temperature (21-24°C) before providing constant flow (0.1μL/min) of Tryptone broth (10g L^{-1}). Media flow was achieved using syringe pumps (Pico Plus Elite, Harvard Apparatus) and 1mL syringes (25-guage needle) fitted with #30 Cole palmer PTFE tubing (ID = 0.3mm). Tubing was inserted into holes bored in the PDMS with a catheter punch driver.

Bacteriophage amplification and purification. T7 phages (18) were used for all experiments. *E coli* AR3110 was used as the phage host for amplification. Purification was conducted according to a protocol developed by Bonilla et al. (66). Briefly, overnight cultures of AR3110 were back diluted 1:10 into 100mL lysogeny broth supplemented with 0.001 M $CaCl_2$ and $MgCl_2$, and incubated for 1 hour at 37°C with shaking; 100μL phage lysate was the added and incubated until the culture cleared completely as assessed by eye. Cultures were pelleted, sterile filtered and treated with chloroform. Chloroform was separated from lysate *via* centrifugation and aspiration of supernatant. Phage lysate was then concentrated and cleaned using phosphate buffered saline and repeated spin cycles of an Amicon® Ultra centrifugal filter units with an Ultracel 200kDa membrane (Millipore Sigma, Burlington MA). Purified phages were stored at 4°C.

Bacteriophage labeling. Phage labeling began with a high titer phage prep ($2x10^{10}$ PFU/mL) produced using the method described above. 900µL of the phage prep was combines with 90µL sodium bicarbonate (1M, pH = 9.0) and 10µL (1mg/mL) amine reactive Alexa-633 probe (ThermoFisher, Waltham MA) and incubated at room temperature for 1 hour. Labeled phage were then dialyzed against 1L phosphate buffered saline to remove excess dye using a Float-A-Lyzer®G2 Dialysis Device MWCO 20kD (Sprectum Labs, Rancho Dominguez CA). Labeled phage were diluted in Tryptone broth ($10gl^{-1}$) to working concentration ($2x10^7$ PFU/mL) prior to use.

Phage-biofilm microfluidic experiments. Biofilms consisting of varying ratios of susceptible and resistant cells were grown in microfluidic devices for 48 hours at room temperature (21-24°C) under constant media flow (tryptone broth $10gl^{-1}$ at 0.1µL/min). Biofilms were imaged immediately prior to phage treatment to establish exact starting ratios of wild type cells (phage-susceptible) and *trxA* deletion mutants (phage-resistant). Subsequently, inlet media tubing was removed from the PDMS microfluidic device and new tubing containing phage diluted in tryptone broth ($2x10^7$ PFU/mL at 0.1µL/min) was inserted. Phage treatment continued for 1 hour, after which original tubing was reinserted to resume flow of fresh tryptone broth without phages. Biofilms were imaged approximately 6, 12, 24 and 48 hours after the conclusion of the phage treatment until a population dynamic steady state was reached.

Imaging and quantification procedures. Biofilms were imaged using a Zeiss LSM 880 confocal microscope with a C-Apochromat 10X/0.45 water objective (Figure 4) or a 40X/1.2 water objective (Figure 5). A 594-nm laser was used to excite mKate2, while a 543-nm laser line was used to excite mKO-κ. Additionally, a 488-nm laser was used to image the phage-encoded GFP fluorescent reporter. A 640-nm laser was used to excite Alexafluor 633. Whole chamber Z stacks were acquired by utilizing 1 X 10 vertical tile scans (total rectangular area ~500x5000µm). Quantification of biomass was performed using customized scripts in MATLAB (MathWorks Natick, MA) as previously described in Drescher et al. 2014 (67) and Nadell et al. 2015 (68).

References

1. Susskind MM, Botstein D (1978) Molecular genetics of bacteriophage P22. *Microbiol Rev* 42(2):385–413.
2. Koskella B, Brockhurst MA (2014) Bacteria–phage coevolution as a driver of ecological and evolutionary processes in microbial communities. *Fems Microbiol Rev* 38(5):916–931.
3. Lenski RE, Levin BR (1985) Constraints on the coevolution of bacteria and virulent phage: a model, some experiments, and predictions for natural communities. *Am Nat*:585–602.
4. Chao L, Levin BR, Stewart FM (1977) A Complex Community in a Simple Habitat: An Experimental Study with Bacteria and Phage. *Ecology* 58(2):369–378.
5. Brockhurst MA, Buckling A, Rainey PB (2006) Spatial heterogeneity and the stability of host-parasite coexistence. *J Evol Biol* 19(2):374–379.
6. Harrison E, Laine A-L, Hietala M, Brockhurst MA (2013) Rapidly fluctuating environments constrain coevolutionary arms races by impeding selective sweeps. *Proc R Soc B* 280(1764):20130937.
7. Brockhurst MA, Buckling A, Rainey PB (2005) The effect of a bacteriophage on diversification of the opportunistic bacterial pathogen, Pseudomonas aeruginosa. *Proc R Soc B* 272(1570):1385–1391.
8. Abedon ST (2008) Bacteriophage Ecology: Population Growth, Evolution, and Impact of Bacterial Viruses.
9. Abedon ST (2011) *Bacteriophages and Biofilms* (Nova Science).
10. Labrie SJ, Samson JE, Moineau S (2010) Bacteriophage resistance mechanisms. *Nat Rev Micro* 8(5):317–327.
11. Samson JE, Magadan AH, Sabri M, Moineau S (2013) Revenge of the phages: defeating bacterial defences. *Nat Rev Micro* 11(10):675–687.
12. Levin BR, Bull JJ (2004) Population and evolutionary dynamics of phage therapy. *Nat Rev Microbiol* 2(2):166–173.
13. Weitz JS, et al. (2013) Phage–bacteria infection networks. *Trends Microbiol* 21(2):82–91.
14. Flemming H-C, Wingender J (2010) The biofilm matrix. *Nat Rev Microbiol* 8:623–633.

15. Flemming H-C, et al. (2016) Biofilms: an emergent form of bacterial life. *Nat Rev Microbiol* 14(9):563–575.
16. Nadell CD, Drescher K, Foster KR (2016) Spatial structure, cooperation, and competition in bacterial biofilms. *Nat Rev Microbiol* 14:589–600.
17. Darch SE, et al. (2017) Phage Inhibit Pathogen Dissemination by Targeting Bacterial Migrants in a Chronic Infection Model. *MBio* 8(2):e00240-17.
18. Vidakovic L, Singh PK, Hartmann R, Nadell CD, Drescher K (2018) Dynamic biofilm architecture confers individual and collective mechanisms of viral protection. *Nat Microbiol* 3:26–31.
19. Davies E V, et al. (2016) Temperate phages both mediate and drive adaptive evolution in pathogen biofilms. *Proc Natl Acad Sci* 113(29):8266–8271.
20. Stewart PS, Franklin MJ (2008) Physiological heterogeneity in biofilms. *Nat Rev Microbiol* 6(3):199–210.
21. Stewart PS (2012) Mini-review: Convection around biofilms. *Biofouling* 28(2):187–198.
22. Mah T-FC, O'Toole GA (2001) Mechanisms of biofilm resistance to antimicrobial agents. *Trends Microbiol* 9(1):34–39.
23. Tseng BS, et al. (2013) The extracellular matrix protects Pseudomonas aeruginosa biofilms by limiting the penetration of tobramycin. *Environ Microbiol* 15(10):2865–2878.
24. Abedon ST, Thomas-Abedon C (2010) Phage Therapy Pharmacology. *Curr Pharm Biotechnol* 11(1):28–47.
25. Chan BK, Abedon ST (2012) Phage Therapy Pharmacology: Phage Cocktails. *Advances in Applied Microbiology, Vol 78*, eds Laskin AI, Sariaslani S, Gadd GM, pp 1–23.
26. Azeredo J, Sutherland IW (2008) The use of phages for the removal of infectious biofilms. *Curr Pharm Biotechnol* 9(4):261–266.
27. Sutherland IW, Hughes KA, Skillman LC, Tait K (2004) The interaction of phage and biofilms. *Fems Microbiol Lett* 232(1):1–6.
28. Simmons M, Drescher K, Nadell CD, Bucci V (2017) Phage mobility is a core determinant of phage–bacteria coexistence in biofilms. *Isme J* 12:531–543.
29. Eriksen RS, Svenningsen SL, Sneppen K, Mitarai N (2018) A growing microcolony can survive and support persistent propagation of virulent phages. *Proc Natl Acad Sci U S A* 115(2):337–342.
30. Chaudhry WN, et al. (2018) Leaky resistance and the conditions for the existence of lytic bacteriophage. *PLOS Biol* 16(8):e2005971.
31. Bull JJ, Vegge CS, Schmerer M, Chaudhry WN, Levin BR (2014) Phenotypic Resistance and the Dynamics of Bacterial Escape from Phage Control. *PLoS One* 9(4):e94690.
32. Xavier JB, Picioreanu C, van Loosdrecht M (2005) A general description of detachment for multidimensional modelling of biofilms. *Biotechnol Bioeng* 91(6):651–669.
33. Picioreanu C, van Loosdrecht MCM, Heijnen JJ (1998) A new combined differential-discrete cellular automaton approach for biofilm modeling: Application for growth in gel beads. *Biotechnol Bioeng* 57(6):718–731.
34. Nadell CD, et al. (2013) Cutting through the complexity of cell collectives. *Proc R Soc B* 280(1755):20122770.
35. Siepielski AM, McPeek MA (2010) On the evidence for species coexistence: a critique of the coexistence program. *Ecology* 91(11):3153–64.
36. Weitz JS, Hartman H, Levin SA (2005) Coevolutionary arms races between bacteria and bacteriophage. *Proc Natl Acad Sci U S A* 102(27):9535–9540.
37. Levin BR, Stewart FM, Chao L (1977) Resource-Limited Growth, Competition, and Predation: A Model and Experimental Studies with Bacteria and Bacteriophage. *Am Nat* 111(977):3–24.
38. Nadell CD, Foster KR, Xavier JB (2010) Emergence of spatial structure in cell groups and the evolution of cooperation. *PLoS Comput Biol* 6(3):e1000716.
39. Mitri S, Clarke E, Foster KR (2015) Resource limitation drives spatial organization in microbial groups. *ISME J*. doi:10.1038/ismej.2015.208.
40. Xavier JB, Picioreanu C, van Loosdrecht MCM (2005) A framework for multidimensional modelling of activity and structure of multispecies biofilms. *Environ Microbiol* 7(8):1085–1103.
41. Picioreanu C, van Loosdrecht MCM, Heijnen JJ (1998) Mathematical modeling of biofilm structure with a hybrid differential-discrete cellular automaton approach. *Biotechnol Bioeng* 58(1):101–116.

42. Hallatschek O, Hersen P, Ramanathan S, Nelson DR (2007) Genetic drift at expanding frontiers promotes gene segregation. *Proc Natl Acad Sci USA* 104(50):19926–19930.
43. Gralka M, et al. (2016) Allele surfing promotes microbial adaptation from standing variation. *Ecol Lett* 19(8):889–898.
44. MacArthur R (1972) *Geographical Ecology* (Princeton University Press, Princeton, NJ).
45. Levin SA (1970) Community Equilibria and Stability, and an Extension of the Competitive Exclusion Principle. *Am Nat* 104(939):413–423.
46. Chesson P (2000) Mechanisms of Maintenance of Species Diversity. *Annu Rev Ecol Syst* 31(1):343–366.
47. Qimron U, Marintcheva B, Tabor S, Richardson CC (2006) Genomewide screens for Escherichia coli genes affecting growth of T7 bacteriophage. *Proc Natl Acad Sci* 103(50):19039–19044.
48. Heilmann S, Sneppen K, Krishna S (2012) Coexistence of phage and bacteria on the boundary of self-organized refuges. *Proc Natl Acad Sci U S A* 109(31):12828–12833.
49. Díaz-Muñoz SL, Koskella B (2014) Bacteria-phage interactions in natural environments. *Adv Appl Microbiol* 89(135):10.1016.
50. Koskella B, Thompson JN, Preston GM, Buckling A (2011) Local biotic environment shapes the spatial scale of bacteriophage adaptation to bacteria. *Am Nat* 177(4):440–451.
51. Koskella B, Meaden S, Koskella B, Meaden S (2013) Understanding Bacteriophage Specificity in Natural Microbial Communities. *Viruses* 5(3):806–823.
52. Kunin V, et al. (2008) A bacterial metapopulation adapts locally to phage predation despite global dispersal. *Genome Res* 18(2):293–7.
53. Fong JC, et al. (2017) Structural dynamics of RbmA governs plasticity of Vibrio cholerae biofilms. *Elife* 6. doi:10.7554/eLife.26163.
54. Singh PK, et al. (2017) Vibrio cholerae Combines Individual and Collective Sensing to Trigger Biofilm Dispersal. *Curr Biol* 27(21):3359–3366.e7.
55. Levin BR, Bull JJ (1996) Phage therapy revisited: The population biology of a bacterial infection and its treatment with bacteriophage and antibiotics. *Am Nat* 147(6):881–898.
56. Sillankorva S, Neubauer P, Azeredo J (2010) Phage control of dual species biofilms of Pseudomonas fluorescens and Staphylococcus lentus. *Biofouling* 26(5):567–575.
57. Harcombe WR, Bull JJ (2005) Impact of phages on two-species bacterial communities. *Appl Environ Microbiol* 71(9):5254–9.
58. Salmond GPC, Fineran PC (2015) A century of the phage: past, present and future. *Nat Rev Micro* 13:777–786.
59. Lardon LA, et al. (2011) iDynoMiCS: next-generation individual-based modelling of biofilms. *Environ Microbiol* 13(9):2416–2434.
60. Bucci V, Hoover S, Hellweger FL (2012) Modeling Adaptive Mutation of Enteric Bacteria in Surface Water Using Agent-Based Methods. *Water, Air, Soil Pollut* 223(5):2035–2049.
61. Hellweger FL, Bucci V (2009) A bunch of tiny individuals-Individual-based modeling for microbes. *Ecol Modell* 220(1):8–22.
62. Bucci V, Nadell CD, Xavier JB (2011) The evolution of bacteriocin production in bacterial biofilms. *Am Nat* 178(6):E162–E173.
63. Datsenko KA, Wanner BL (2000) One-step inactivation of chromosomal genes in Escherichia coli K-12 using PCR products. *Proc Natl Acad Sci U S A* 97(12):6640–5.
64. Weibel DB, DiLuzio WR, Whitesides GM (2007) Microfabrication meets microbiology. *Nat Rev Microbiol* 5(3):209–218.
65. Sia SK, Whitesides GM (2003) Microfluidic devices fabricated in poly(dimethylsiloxane) for biological studies. *Electrophoresis* 24:3563–3576.
66. Bonilla N, et al. (2016) Phage on tap–a quick and efficient protocol for the preparation of bacteriophage laboratory stocks. *PeerJ* 4:e2261.
67. Drescher K, Nadell CD, Stone HA, Wingreen NS, Bassler BL (2014) Solutions to the Public Goods Dilemma in Bacterial Biofilms. *Curr Biol* 24(1):50–55.
68. Nadell CD, Drescher K, Wingreen NS, Bassler BL (2015) Extracellular matrix structure governs invasion resistance in bacterial biofilms. *ISME J* 9:1700–1709.
69. McCarty PL (2012) *Environmental biotechnology: principles and applications* (Tata McGraw-Hill

Education).
70. Stewart P (2003) Diffusion in Biofilms. *J Bacteriol* 185(5):1485–1491.
71. Henze M, Grady Jr CPL, Gujer W, Marais GVR, Matsuo T (1987) Activated sludge model no. 1: Iawprc scientific and technical report no. 1. *IAWPRC, London*.
72. Henze M, et al. (1999) Activated Sludge Model No.2d, ASM2d. *Water Sci Technol* 39(1):165–182.
73. Oliveira CS, et al. (2009) Determination of kinetic and stoichiometric parameters of Pseudomonas putida F1 by chemostat and in situ pulse respirometry. *Chem Prod Process Model* 4(2).
74. Loferer-Krößbacher M, Klima J, Psenner R (1998) Determination of Bacterial Cell Dry Mass by Transmission Electron Microscopy and Densitometric Image Analysis. *Appl Environ Microbiol* 64(2):688–694.
75. Laspidou CS, Rittmann BE (2002) Non-steady state modeling of extracellular polymeric substances, soluble microbial products, and active and inert biomass. *Water Res* 36(8):1983–1992.
76. Narang A, Konopka A, Ramkrishna D (1997) New patterns of mixed-substrate utilization during batch growth of Escherichia coli K12. *Biotechnol Bioeng* 55(5):747–757.
77. Beg QK, et al. (2007) Intracellular crowding defines the mode and sequence of substrate uptake by Escherichia coli and constrains its metabolic activity. *Proc Natl Acad Sci* 104(31):12663–12668.
78. Trojanowicz K, Styka W, Baczynski T (2009) Experimental determination of kinetic parameters for heterotrophic microorganisms in biofilm under petrochemical wastewater conditions. *Polish J Environ Stud* 18(5).
79. Laspidou CS, Rittmann BE (2004) Modeling the development of biofilm density including active bacteria, inert biomass, and extracellular polymeric substances. *Water Res* 38(14–15):3349–3361.
80. Esquivel-Rios I, et al. (2014) A microrespirometric method for the determination of stoichiometric and kinetic parameters of heterotrophic and autotrophic cultures. *Biochem Eng J* 83:70–78.
81. Abedon ST (2009) Kinetics of Phage-Mediated Biocontrol of Bacteria. *Foodborne Pathog Dis* 6(7):807–815.
82. Endy D, You L, Yin J, Molineux IJ (2000) Computation, prediction, and experimental tests of fitness for bacteriophage T7 mutants with permuted genomes. *Proc Natl Acad Sci* 97(10):5375–5380.
83. Delbrück M (1945) The burst size distribution in the growth of bacterial viruses (bacteriophages). *J Bacteriol* 50(2):131.

Supplemental Information

Evolutionary dynamics of phage resistance in bacterial biofilms

Matthew Simmons[1,2†], Matthew C. Bond[2†], Knut Drescher[3,4], Vanni Bucci[1]*, Carey D. Nadell[2]*

[1] Department of Bioengineering, Program in Biotechnology and Biomedical Engineering, University of Massachusetts Dartmouth, N. Dartmouth, MA 02747, USA

[2] Department of Biological Sciences, Dartmouth College, Hanover, NH 03755, USA

[3] Max Planck Institute for Terrestrial Microbiology, D-35043 Marburg, Germany

[4] Department of Physics, Philipps-Universität Marburg, D-35032 Marburg, Germany

† Co-first authors

* Authors for correspondence:

Carey Nadell (carey.d.nadell@dartmouth.edu)
Vanni Bucci (vanni.bucci@umassd.edu)

Supplementary Table 1: Model Parameters used for Simulations

Parameter	Value used in the simulations			Description	References where applicable	Representative value ranges and additional references, where applicable
x_{max},y_{max}	$750\ \mu m, 750\ \mu m$			The physical size of the system	N/A	
dl, dV	$3\ \mu m, 27\ \mu m^3$			Length and volume of a grid element	N/A	
N_{max}, D_N, h	Low $10\ mg\ L^{-1}$ 2.3e-6 $cm^2\ s^{-1}$ $100\ um$	Mid 15 1.2e-5 100	Max 0.25 N/A N/A	Maximum density of substrate (range of values investigated in this study)	(69)	
N_{max}	$0.043\ mg\ L^{-1}$	0.185	0.22	Well-mixed simulation nutrient availability	(70)	
K_N	$1.18\ mg\ L^{-1}$			Half saturation constant for substrate	(40, 71)	5 - 225 Biofilm heterotrophic bacterial biomass, including fecal coliforms, e.g. *E. coli* (71, 72) 4.86 *Pseudomonas putida* F1 on glucose (73)
δ_E	$1.61\ (m\ h)^{-1}$			Erosion constant	(32)	-
m_s	$10^{-12} g$			Bacterial mass per cell	(74)	10^{-12} *E. coli* DSM 613
δ_d	$0.0792\ day^{-1}$			Decay to inert mass constant	(71)	Biofilm heterotrophic bacterial biomass, including fecal coliforms, e.g. *E. coli*
μ_s (*)	$14.1\ day^{-1}$			Maximum growth rate	(75)	17. *8* *E. coli* K-12 on glucose (76) 4.8-17.6 *E. coli* K-12 on different substrates (77)

				6.1 Wastewater heterotrophic bacterial biomass (78)
S_{max}	$200\ g\ L^{-1}$	Maximum active biomass density	(79)	-
Y	0.495	Yield of substrate converted to biomass	(62)	0.69-0.77 Wastewater bacteria (80) 0.41 *E. coli* K-12 on glucose (76) 0.41-0.51 *P. putida* F1 on glucose (73)
β	120	Phage burst size	(81–83)	Bacteriophage T7
D_P	$3.82 * 10^{-7}$ $cm^2\ s^{-1}$	Phage diffusivity constant	(8, 81)	Bacteriophage T7
I	$0.347 - 9.25\ s^{-1}$	Rate of interaction of phage particles with biomass particles	This Study	-
τ	$28.8\ minutes$	Incubation period before lysis	(8, 81)	Bacteriophage T7
γ	$2.92\ h^{-1}$	Infection rate per biomass per phage		-

(*) The max growth rate is determined from the model equations as $\mu_s = q_s Y$. q_s is the substrate uptake rate with value $28.5\ g\ day^{-1}$ as in Lapisdou et al. (75)

Supplemental Figures

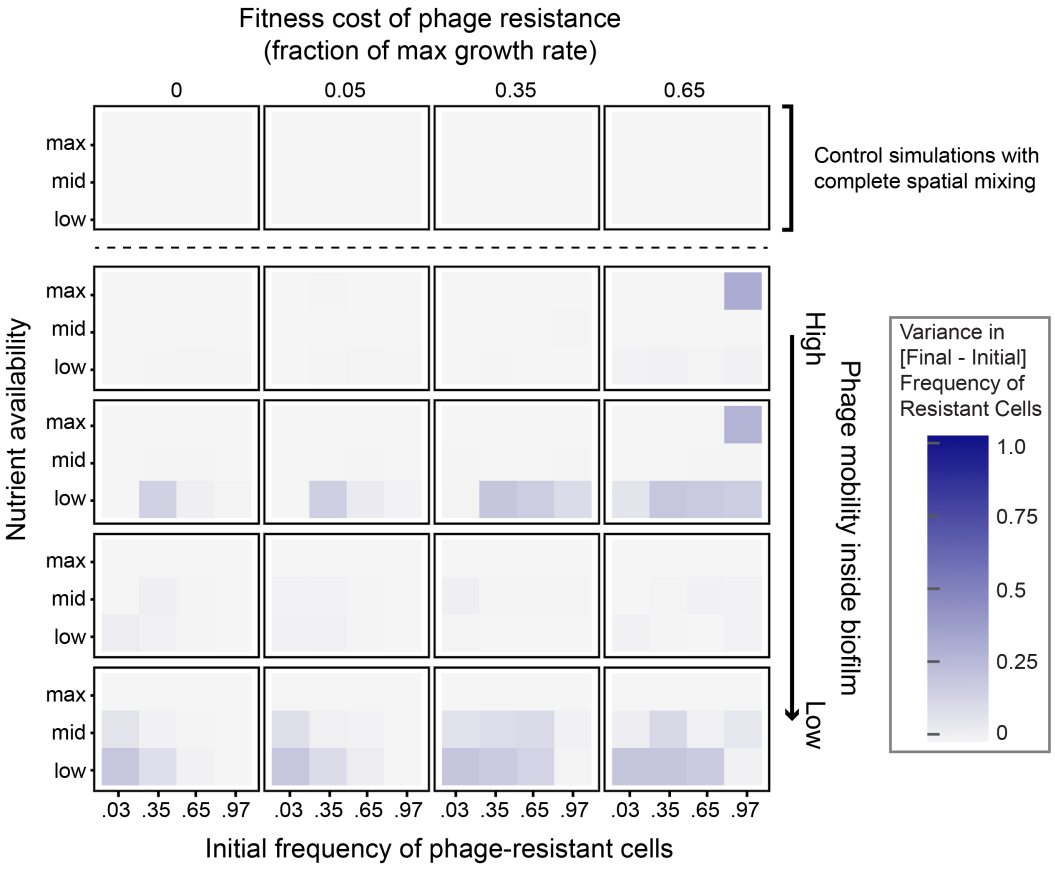

Figure S1. Variance in simulation results from major parameter sweep of phage-biofilm interactions. Parameters and their ranges are identical to those in Figure 1 of the main text, but here the variance in the change in frequency of the resistant strain is shown across all parameter combinations. Note that the variance in outcome was low for the majority of simulation sets, increasing only for the lowest nutrient conditions in which typical biofilm population sizes were smaller than those in the "mid" or "max" nutrient conditions, and thus more heavily influenced by genetic drift.

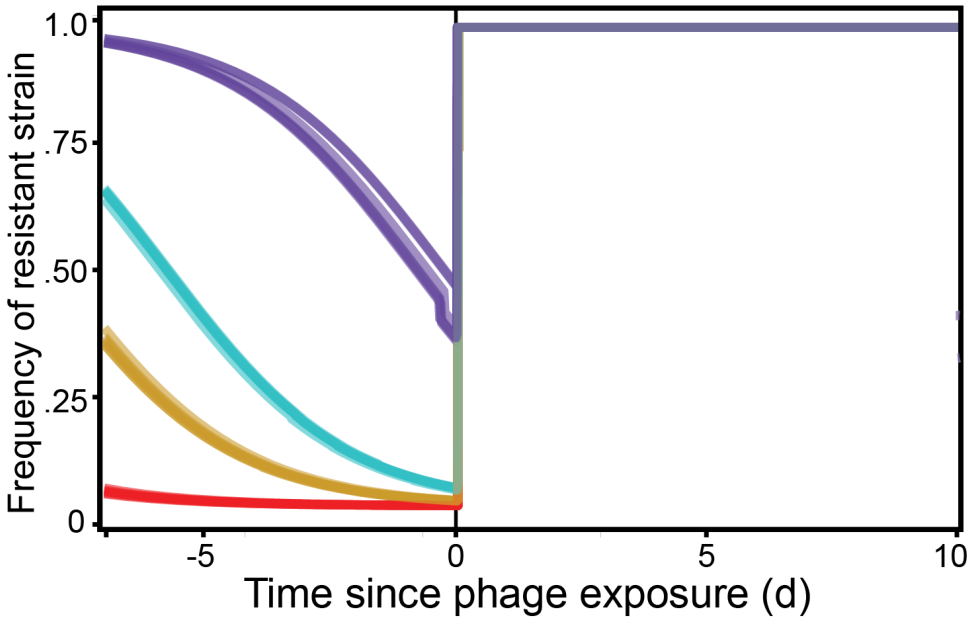

Figure S2. Population dynamics of phage-resistant and phage-susceptible cells in an implementation of our simulation models in well-mixed conditions. The frequency of resistant cells is shown from different starting conditions; varying trace colors correspond to the initial frequency of resistant cells (red: 0.05; orange: 0.35; teal: 0.65; purple: 0.95) and are meant to assist in visualization and comparison with Figures 2-4 in the main text. For the runs shown here, the fitness cost of phage resistance is 0.35, and all bacteria and phages interact randomly with each other at every time step. In these conditions, here shown with a fitness cost for resistance of 35% of the maximum growth rate, resistant cells decline in relative abundance due to slower growth rate, until phages are introduced (indicated by the 0 time point). After phages are introduced, all susceptible cells are quickly killed. Resistant cells go to fixation for all initial conditions, in contrast to the outcome for biofilm simulations and experiments (see main text).

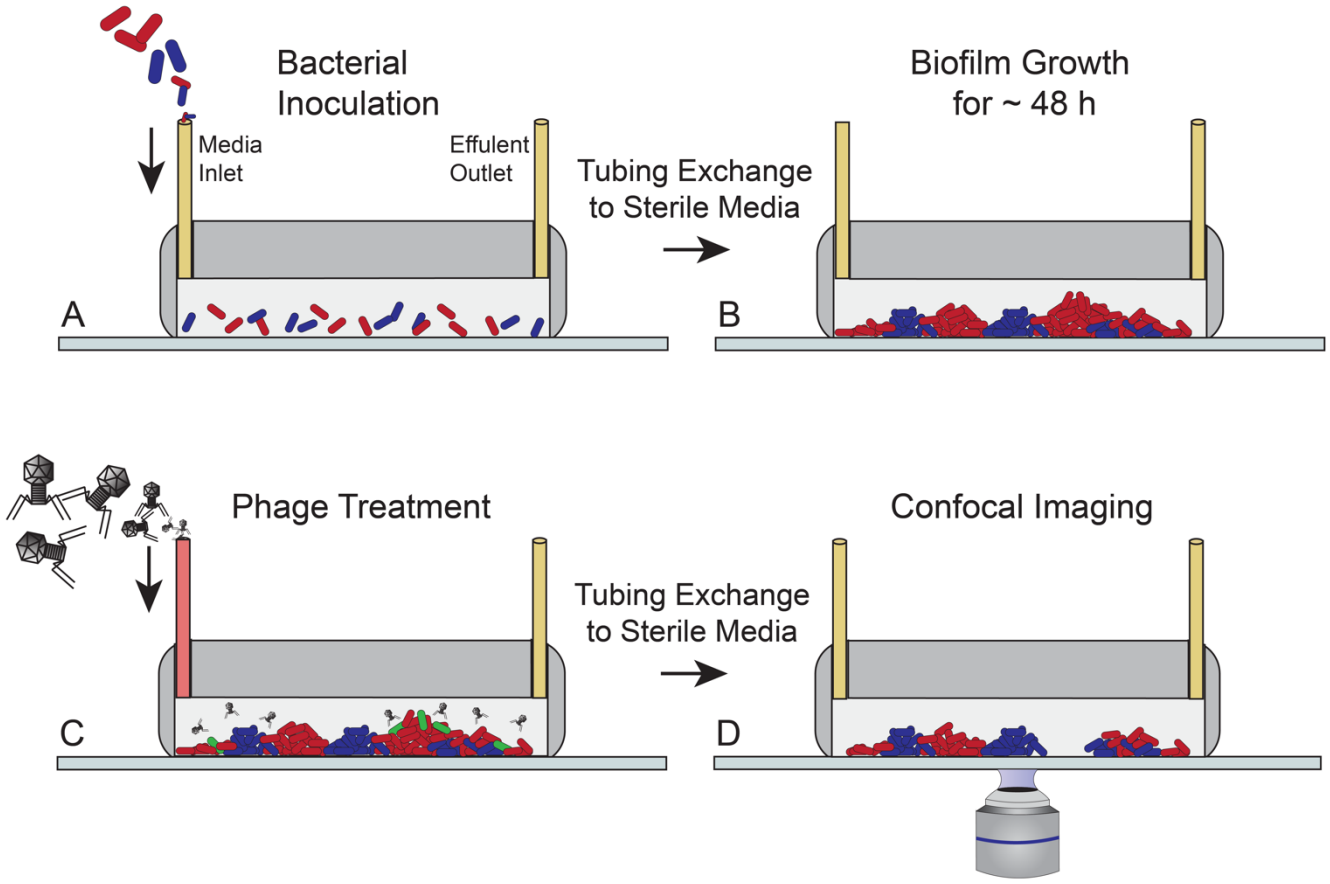

Figure S3. Diagram of experimental biofilm growth and phage treatment regime. A) Biofilms were grown by inoculating phage-susceptible and -resistant cells in controlled ratios (see main text) onto the glass bottom of PDMS microfluidic devices. B) Biofilms were grown in the absence of phage for 48 hours, after which (C) the medium inlet tubing was switched to perfuse biofilms with T7 phages. (D) the inlet tubing was replaced again to continue flow of fresh media, and image series were acquired by confocal microscopy.

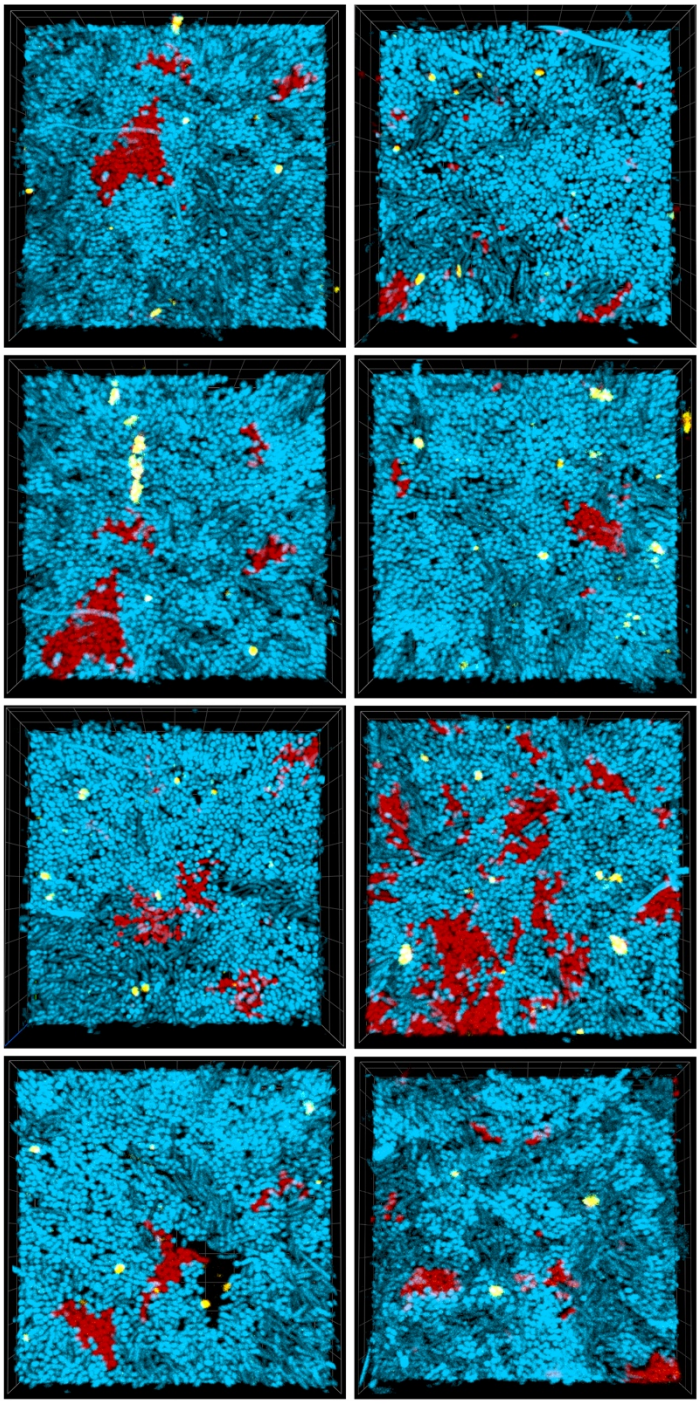

Figure S4. Phages (yellow) trapped by majority resistant bacteria (blue) are unable to reach and infect sparse patches of susceptible cells (red). Additional replicates of the experiment depicted in Figure 5 of the main text, in which biofilms inoculated with 20:1 resistant-susceptible cells were grown for 48 hours and then pulsed with phages for prior to imaging by confocal microscopy. Each panel above is a 3-D biofilm volume rendering ~ 50µm x 50µm x 15 µm [L x W x D].

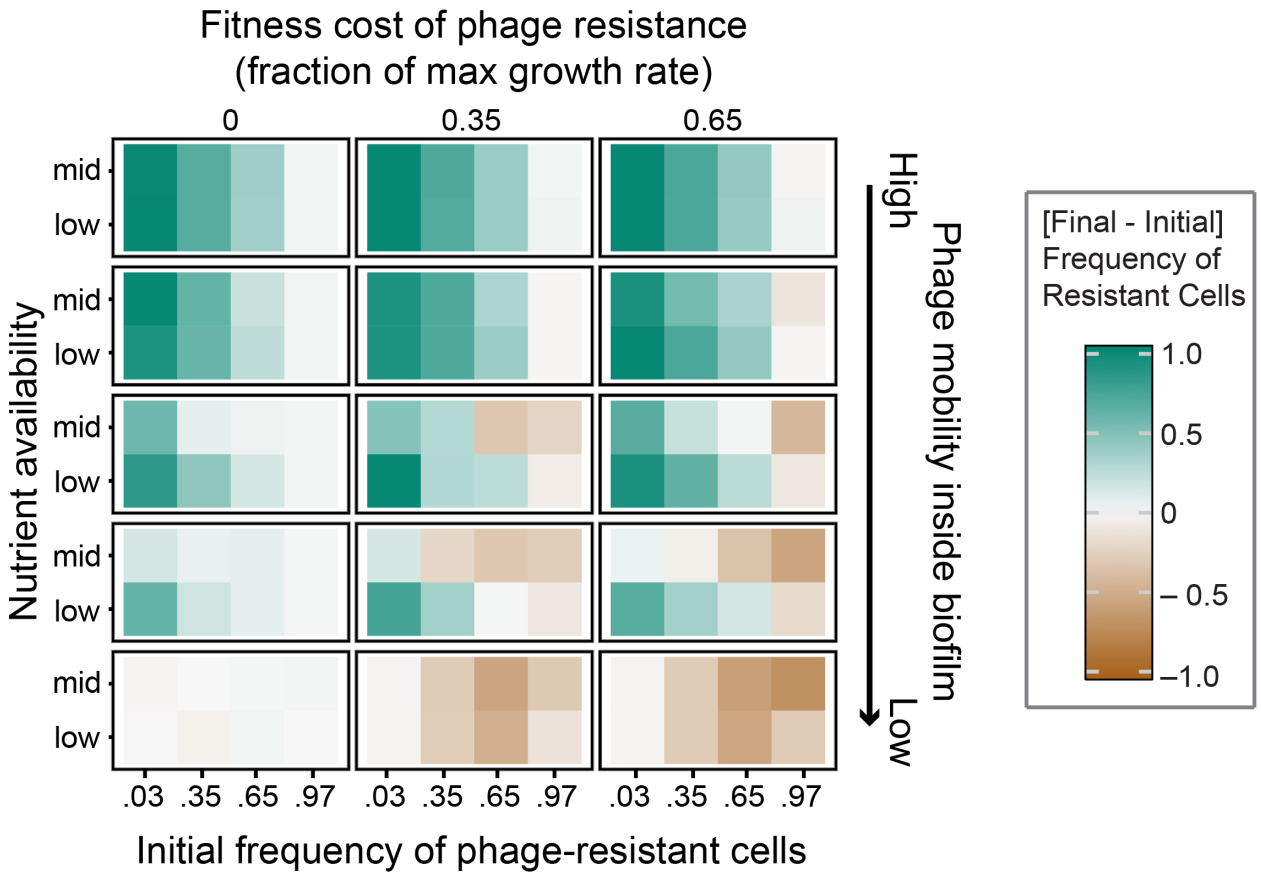

Figure S5. Inoculating phages early during biofilm growth does not significantly affect simulation outcomes. A subset of the simulations summarized in Figure 1 of the main text were repeated with earlier addition of phages to the system (we did not include well-mixed controls or simulations corresponding to the 'max' nutrient condition, neither of which showed any significant variation in outcome with phage treatment timing during pilot experiments). No qualitative changes in mean simulation outcome were observed.

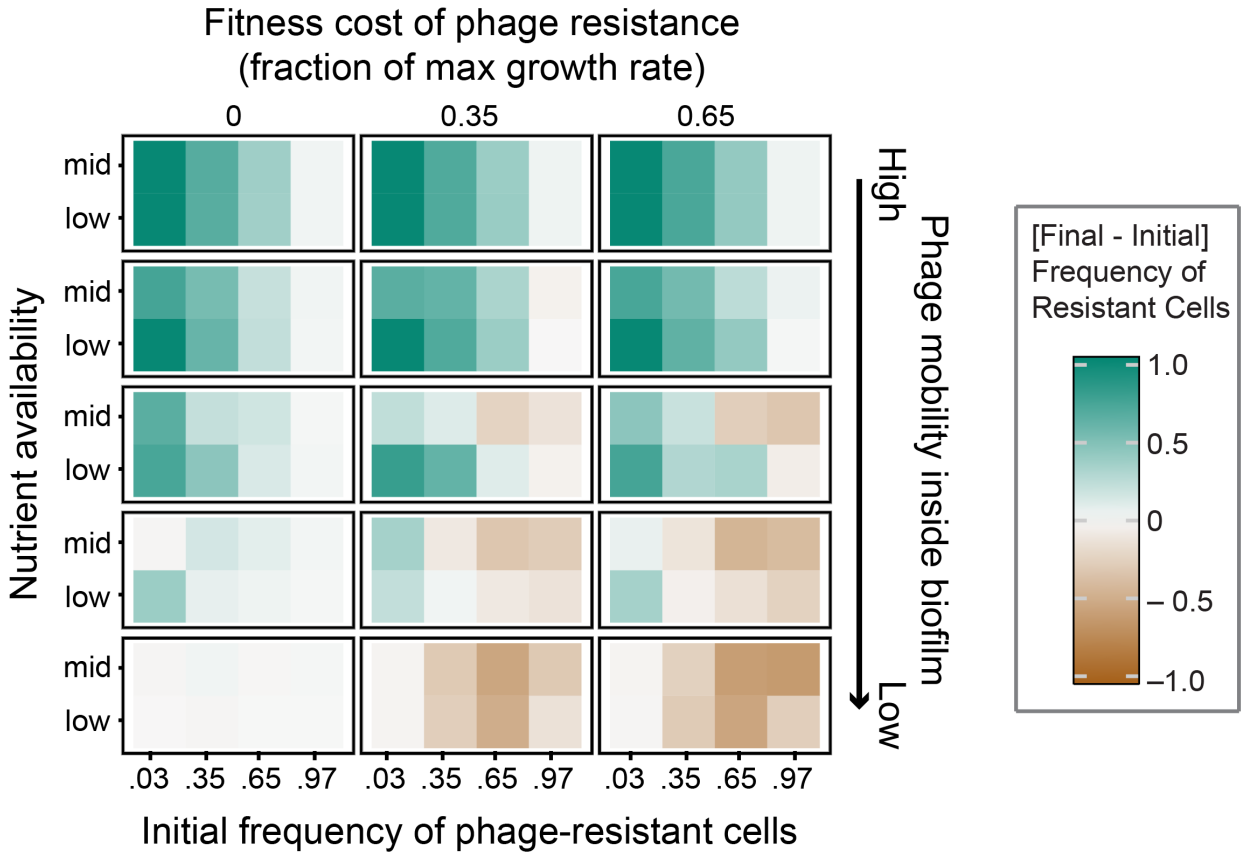

Figure S6. Inoculating phages late during biofilm growth does not significantly affect simulation outcomes. The simulations summarized in Figure S5 were repeated with later addition of phages to the system. No qualitative changes in mean simulation outcome were observed.

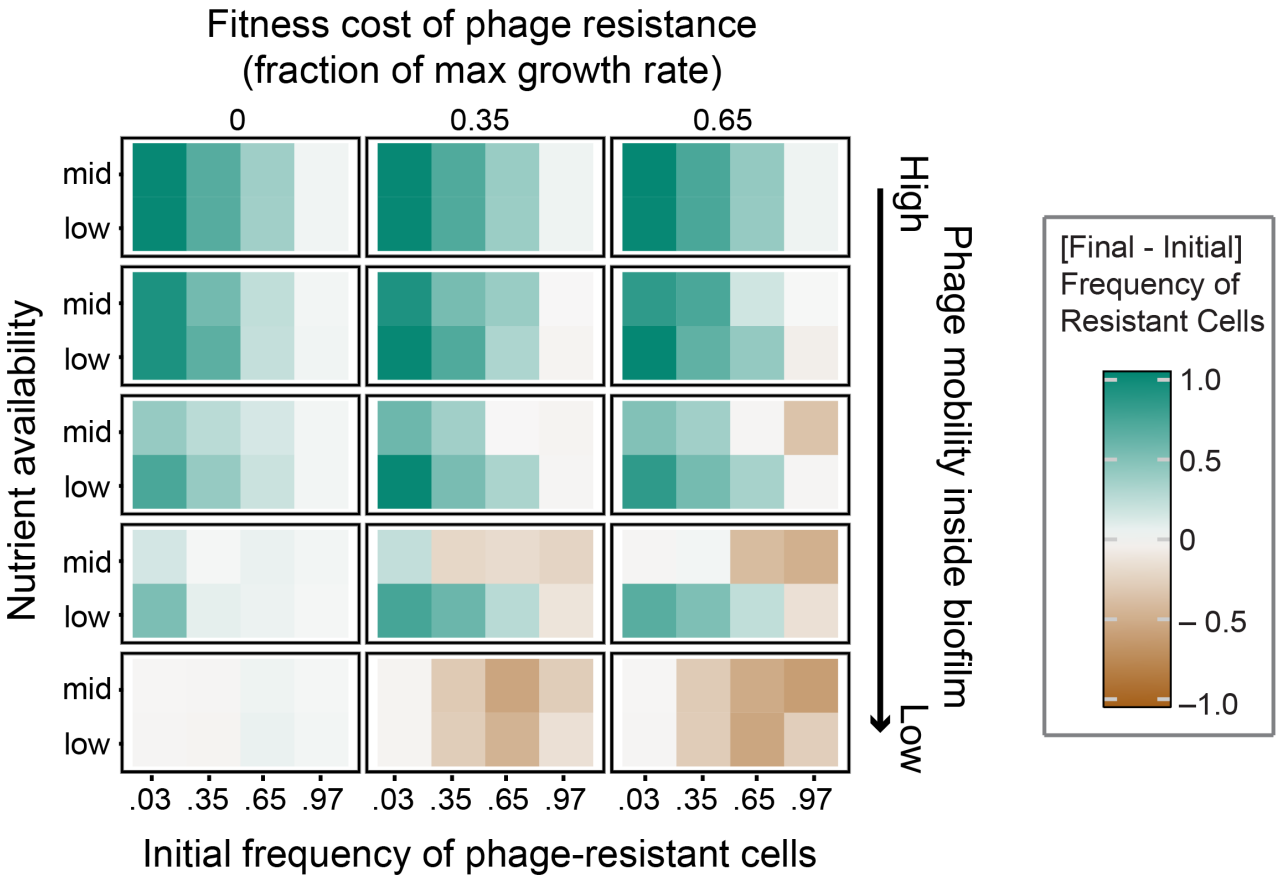

Figure S7. Inoculating phages at a single spatial location near the biofilm surface, instead of evenly distributed over the biofilm. The simulations summarized in Figure S5 were repeated with addition of phages at a single location randomly chosen above the biofilm surface, instead of equally spread over the biofilm surface as in Figure 1 of the main text. No qualitative changes in mean simulation outcomes were observed.

Supplemental Videos

SI Video 1: A simulation corresponding to conditions where nutrient supply is saturating (denoted by "max" in Figure 1 of main text). The biofilm is growing with a uniform front. Phage-susceptible bacteria are shown in red, -resistant in blue, -infected bacteria are shown in green, and phages are shown in black. As the biofilm expands much faster than phage infections can kill susceptible cells, phage predation does not impose a substantial influence on population composition. As the cost of resistance is 0, phage-susceptible and -resistant bacteria have equal fitness with the consequence that the relative ratio at the end of the simulation remains the same as at the beginning.

SI Video 2: A simulation corresponding to conditions where nutrient supply is saturating (denoted by "max" in Figure 1 of main text). The biofilm is growing as a uniform front. Compared to SI Video 1, the phage-resistant strain (blue) suffer cost of resistance. As a consequence, the resistant strain suffers a lower growth rate and is selected against. Phage-susceptible bacteria are shown in red, -resistant in blue, -infected bacteria are shown in green, and phages are shown in black.

SI Video 3: A simulation corresponding to conditions where nutrient supply is intermediate (denoted by "mid" in Figure 1 of main text). The biofilm is growing as tower-like structures. This simulation displays an instance of the clearance effect, in which phage-resistant bacteria that start as a rare minority take-over the biofilm population after the introduced phages clear most of the phage-susceptible population. Phage-susceptible bacteria are shown in red, -resistant in blue, -infected bacteria are shown in green, and phages are shown in black.

SI Video 4: A simulation corresponding to conditions where nutrient supply is intermediate (denoted by "mid" in Figure 1 of main text). The biofilm is growing as tower-like structures. This simulation displays an instance of phage blocking, in which phage-resistant bacteria towers act as shield allowing phage-susceptible towers to grow undisturbed (see Main text). Phage-susceptible bacteria are shown in red, -resistant in blue, -infected bacteria are shown in green, and phages are shown in black.